

# Dynamic Fragmentation of Planetary Materials: Length Scale Quantification and Semi-Analytical Modelling

James D. Hogan<sup>a,b</sup>, John G. Spray<sup>b</sup>, Robert J. Rogers<sup>a</sup>

<sup>a</sup>*Department of Mechanical Engineering, University of New Brunswick, Fredericton, New Brunswick E3B 5A3, Canada*

<sup>b</sup>*Planetary and Space Science Centre, University of New Brunswick, Fredericton, New Brunswick E3B 5A3, Canada*

---

## Abstract

The dynamic fragmentation of planetary materials has been examined. A particle tracking algorithm was implemented to estimate ejecta size and velocity at the rear of the target. A total of 76 experiments were performed for four material, target thicknesses of 7 mm to 55 mm, and impact energies of 10 J to 6,350 J. Semi-empirical models were developed from non-dimensional groups to predict key experimental results. These include the amount of material ejected from the target, and the transformation of incoming projectile kinetic energy to the total ejecta kinetic energy. The amount of impact energy converted to kinetic energy of ejecta was found to increase from 2% to 18 % for increasing non-dimensional impact energy. Energy dissipated into expanding the field laterally was found to be small in comparison to the streamwise direction ( $\sum KE_y / \sum KE_x = 4\%$ ).

Percentile length scales describing the contribution of mass, momentum and kinetic energy were also examined. Length scales decrease for increasing normalized impact energy. Fits of the non-dimensional length scale groups provide

---

*Email address:* [jd.hogan@unb.ca](mailto:jd.hogan@unb.ca) (James D. Hogan)

reasonable collapse for the percentile values. Lastly, the cumulative distributions of mass, momentum and kinetic energy among normalized lengths (i.e., normalized by 50 % length values) were quantified. Exponential function forms were found to fit all of the data over the range over normalized length scales of 0.3 to 4. When integrated, this predicts the probability density distribution of mass, momentum, and kinetic energy among ejecta lengths.

*Keywords:* dynamic fragmentation, particle tracking, brittle fracture, impact testing, length scales, energy dissipation, planetary materials

---

## **1. Introduction**

The complex dynamic response of planetary materials (e.g., rocks) subject to impact arises from the poorly understood interactions of material properties and resulting fracture behaviours under multi-axial stress states. During dynamic fragmentation, fracture initiates at pre-existing flaws and propagates in response to local tensile stresses acting perpendicular to the crack plane [1]. This failure propagates at the bulk scale down to the micro scale, resulting in a cascade of plastic and thermal effects [2]. Understanding the dynamic fragmentation of planetary materials is important in seismology and earthquake science [3], volcanology [4], and, more applicable to the this work, planetary and space science and the formation of ejecta clouds during impact [5–8].

Planetary materials are commonly brittle and the strain rate of loading is influential during their dynamic fragmentation. At low to moderate strain rates ( $250 \text{ s}^{-1}$  to  $25,000 \text{ s}^{-1}$ ), the distribution of defects controls fragmentation [9]. At higher strain rates (approximately  $> 25,000 \text{ s}^{-1}$ ), fragmentation is mainly a kinetic process and the influence of internal defects is negligible [10]. A direct

result of fragmentation at high strain rates is that the failure strength increases and becomes less stochastic [11, 12]. It is worth noting that at high strain rates, the initial fragmentation process only represents a fraction of the final number of fragments generated during loading [13]. The majority of fragmentation (in terms of generation and number) occurs via comminution of fractured surfaces [14].

The partitioning of initial impact energy into fragmentation (or fracture) energy, kinetic energy, heat, acoustic emissions, and elastic strain energy remains difficult to access. Efficiencies<sup>1</sup> of  $\sim 1\%$  to  $\sim 2\%$  [16–18] have been reported for fragmentation energy. Similar conversion rates have been reported during impact tests [19, 20]. Higher efficiencies ( $\sim 15\%$ ) are estimated when the ratio of energy required for single particle fracture to mechanical input energy is considered instead of the ratio of the energy of creating new surface area to mechanical energy [15]. Acoustic emissions account for approximately 3% of energy during fracture [21]. Upwards of  $\sim 26\%$  of impact energy can be transformed to heat generated via friction in high speed ( $>6$  km/s) impact experiments into granular media [22]. Thermal dissipation likely accounts for more than this as it is believed to represent 99% of the amount of energy that is dissipated into fracture (with 1 % going into making the new surface) [23, 24]. In impact tests into solid planetary materials, a significant amount of heat is generated via shearing of adjacent fracture surfaces [20]. It is difficult the total conversion of impact energy to heat, but is believed to be the greatest source of energy dissipation.

In an extensive study on energy partitioning in rock blasting, Sanchidrian et al. [25] noted that 2 % to 6 % of the total energy is converted to fragmentation

---

<sup>1</sup>Defined as the ratio of fracture surface area energy generated to mechanical strain energy input [15].

energy, 1 % to 3 % to seismic energy (i.e., elastic energy) and 3 % to 21 % for kinetic energy. The remaining is likely dissipated into heat. Energy partitioning in hypervelocity impact was investigated, primarily using 1-dimensional wave calculation code, in an early study by Gault and Heitowit [26]. They noted that <1 % is converted to elastic wave, 19 % to 23 % of impact energy is converted to waste heat, 10 % to 24 % converted to comminution (i.e., fragmentation), and 43 % to 53 % was converted to ejecta translational kinetic energy. The conversion of impact energy to translational kinetic energy is investigated in this paper. The distribution of this energy among ejecta sizes is also considered.

There have been numerous analytical models predicting average fragment size during the dynamic fragmentation of brittle materials. In one class of theories, geometric statistical considerations are used to predict the distribution of fragment sizes [27, 28]. Grady [29] derived predictive capabilities for average fragment size based on an energy balance between the surface energy released due to fracture and the kinetic energy of the fragments. Glenn and Chudnovsky [30] refined the Grady model to account for the strain energy of the fragments. The major limitations of energy models arise from accurately determining how much of the total energy is dissipated into the generation of new surfaces. Models have also been proposed based on numerical simulations, which involve cohesive finite element schemes [31] that can account for, as an example, material flaw distribution [32, 33]. Zhou et al.[34] have successfully implemented these schemes and developed fragment prediction models for three-dimensional fragmentation scenarios. These models are explored further in the paper.

This paper examines length scales in the dynamic fragmentation of planetary materials. It is a part of a broader study by Hogan et al. [2, 14, 20, 35] to

characterize the high rate behaviour of geological materials during impact. Two important stages of impacts are quantified: (1) fragmentation and (2) material ejection. To date, this work has been primarily focused on characterizing micro-scale failure processes (e.g., thermal and fracture effects [2, 14, 20]) and quantifying fragmentation distributions using innovative particle sizing technologies and methods [2, 14]. Fragmentation results have been shown to have good agreement with theoretical models of fragment sizes (e.g., Grady [29], Zhou et al. [34]). In a more recent paper (Hogan et al. [35]), ejecta velocity, size, mass, momentum and kinetic energy distributions during dynamic fragmentation of gabbro have been examined. Ejecta measurements were made using a developed particle tracking algorithm. Ejecta measurements are limited in the literature due to the challenging nature of the experiment (i.e., triggering and camera resolution) and associated difficulty in developing the track algorithm. This algorithm is also used here. Impact velocities ranged between 25 m/s and 100 m/s and the target thickness was 10 mm. Since this work, image enhancement and post-processing improvements have been made to the tracking algorithm. Algorithm improvements are also outlined in this paper. An additional 57 experiments for three new materials, six target thickness (7 mm to 55 mm) and impact velocities of 20 m/s to 550 m/s have been performed. In the present investigation, the contributions of mass, momentum, and kinetic energy among ejecta lengths are considered for all 76 data sets. Fragmentation distributions are compared with theoretical prediction of average fragment sizes. In a subsequent study under preparation, the focus is on the distribution of mass, momentum, and kinetic energy among ejecta velocities. Combined, these approaches allow detailed consideration of two important stages of impacts into planetary materials: fragmentation (through quantification of ejecta

lengths) and material ejection (through quantification of ejecta velocities).

Semi-empirical non-dimensional scaling relationships are developed to collapse results for the 76 data sets. The development of fitted non-dimensional groups allows results to be viewed in a broader context by incorporating varying and important experimental conditions (e.g., target thickness, material type, and impact energy). These models can be extrapolated to predict the distribution of mass, momentum and kinetic energy among length scales for other brittle materials across a range of impact energies. It also provides reference for those numerically simulating these complex multi-scale events. Examples are explored further in the paper.

## **2. Experimental Setup and Analysis Methods**

The impact tests were performed at the French-German Research Institute of Saint-Louis (ISL), France. Materials, target thickness, velocities and impact energies are given in Table 1. Materials include a finer grained tonalitic granitoid, gabbro, a finer grained syenitic granitoid, and a coarse grained monzonitic granitoid. Photographs of the target materials and projectiles are shown in Figure 1. Composite projectiles (45 g) were used for the syenitic granitoid and aluminum projectiles (65 g) were used for the tonalite, monzonite and gabbro materials. Projectiles are shown in Figure 1e.

### *2.1. Particle Tracking Algorithm*

A tracking algorithm written in Matlab [36] is implemented to track ejecta larger than 1 mm (determined as 3 pixels by the resolution of the camera) over multiple Photron APX Ultima high-speed camera images. The capture rate was 8 kHz. Ejecta were made distinguishable through background subtraction and

image enhancements. Shown in Figure 2 is an example of a high-speed image for the tonalitic rich material impacted at 20 m/s and a target thickness of 10 mm. Measurements are taken when the debris cloud has the greatest expansion in the field of the view of the camera so as to record the most possible fragments. The filtered and enhanced image is shown in b. Probable match (i.e., cross-correlation) between consecutive enhanced high-speed video frames, in conjunction with penalty functions of fragment sizes, shape and circularity, are used to identify fragments. The displacement of the particle over the time between consecutive frames yields velocity. Estimates of fragment masses are obtained by multiplying the two-dimensional projected area with the minor axis dimension (defined as perpendicular to the largest spanning dimension) and density. Individual ejecta momentum and kinetic energy are then estimated. Examples of velocity vectors are shown in Figure 2c. The ejection angle,  $\theta$ , is also defined.

Particle tracking methods applied here have been used in Hogan et al. [35]. Other methods have been used in the past to estimate ejecta velocity, including hand-tracing vector fields on photographs [37, 38], penetrating foils [39], and mass bins downstream [40]. These previous measurements have been limited in the total number of experiments due to the associated cost and difficulty in performing high-speed image experiments, limited in the total number of ejecta appraised when velocities are recorded and, when performed, in combined ejecta size (or mass) and velocity measurements. Challenges in obtaining these measurements are associated with cluttered debris fields, lack of computational power, camera resolution and triggering (e.g., laser sheet with proper field expansion). No published data exists for solid targets at the velocities reported in this paper.

Limitations of the algorithm and experimental measurements are discussed in

brief. The total number of fragments, especially the sub-mm fragments, in this type of measurement is limited by camera resolution and the two-dimensional projection of the field in the high-speed video image. For example, fragments may be hidden in the image. These limitations are expected when performing ejecta measurements in highly cluttered debris fields. The ability to track a representable amount of mass is also considered. For all cases, over 85 % of the mass (i.e., the collected mass of ejecta after experimentation) is tracked by the algorithm. It is believed that methods employed here provide the greatest possibility to achieve an almost complete set among all other techniques and experimental configurations.

The effect of sub-mm fragments is briefly considered. Recent particle size measurements of collected ejecta from these experiments by Hogan et al. [14] have shown that, while fragments smaller 1 mm represent > 99 % of the total number of fragments, they contain less than 1 % of the volume (or mass). The majority of these smaller fragments are formed ahead of the projectile and, therefore, have low ejection velocities. From experimental results to come, it is deduced that ejecta < 1 mm contribute less than 1 % to the total ejecta mass, momentum and kinetic energy. From this, it is assumed that they can be neglected when developing semi-empirical models predicting distributions of mass and kinetic energy among ejecta size.

### **3. Experimental Results**

Dimensionless groups are formed using Buckingham Pi theorem [41] and are fitted with coefficients in an attempt to collapse experimental results. Experimental data sets include 19 experiments involving gabbro tiles (10 mm thick), 9 experiments involving a coarse monzonitic and fine grained syenitic granitoid

blocks, and 48 additional experiments in an tonalitic granitoid material (7 mm to 40 mm thick). An attempt is made here to consider input parameters that, when altered, affect the experimental results. Target thickness,  $t$ , is varied during experimentation and is considered influential during the fragmentation and ejection of the target material. It is taken here as the characteristic length term. Projectile length is taken as the characteristic length parameter in Housen and Holsapple [5] to normalize the radial distance,  $R$ , from the impact point in hypervelocity vertical impacts. In horizontal impacts into non semi-infinite targets (e.g., ballistics applications), projectile length may be considered important as its size affects the time for shock wave propagation within a body. Different behaviours are observed (e.g., disintegration of projectile) when the shock wave propagation time is less in the projectile than in the target. Different material behaviours are also observed when impact speeds are greater than the speed of sound in the target. Projectile length is not considered here as impact speeds are lower than shock speeds and its length does not vary among the present experiments.

The input energy (i.e., impact kinetic energy  $KE$ ) is also considered important during fragmentation and ejection processes in impact events. Kinetic energy incorporates projectile dimensions (e.g., length, density, and velocity), and is used here as a simplification to reduce the total number of non-dimensional groups. At higher impact velocities, projectile density may be considered more important as target-projectile density mismatches affect shock wave generation at impact. Shown in Table 1 is a summary of target thicknesses and impact energies for all experimental trials.

Target properties, such as density ( $\rho$ ), yield strength ( $Y$ ) and fracture toughness ( $K_{IC}$ ) are important during the dynamic fracture of planetary materials and are

considered here as inputs for non-dimensional groups. These are also common materials properties in theoretical predictions of dominant size during fragmentation (e.g., Grady [29]; Zhou et al. [34]). Under the experimental conditions used here, target density represents a quantifier of material composition (e.g., materials with a greater quartz composition will be more dense, at least for those minerals present in the studied targets) and compactness (e.g., similar feldspar-rich materials will have different densities if more flaws are present). Yield strength characterizes the ability of the target to deform before failure and fracture toughness is an indicator of post-failure (i.e., fracture) behaviour. Again, these are chosen because they are important during fragmentation.

Shown in Table 2 is a summary of target density, yield strength and fracture toughness. Material properties are similar for all materials; a reality of choosing solid geological targets.

Housen and Holsapple [5] discuss the challenges associated with choosing an appropriate strength parameter (e.g., yield strength or shear strength). Further complications arise when assigning values for these inputs as limited data exists in the literature for planetary materials. Tensile yield strength values are chosen here because brittle materials typically fail in tension. The effect of loading rate (units: 1/s), which can be estimated as the ratio of impact velocity and target thickness, on material properties is not considered in the current paper. Regardless, these properties vary slightly among the considered materials and are believed to be important in the dynamic fragmentation of planetary materials. A study involving a broader range of planetary materials (e.g., porous materials) or other brittle materials (e.g., boron carbide) would provide a greater insight into the effect of, for example, yield strength. There are many choices for input parameters and the

selection of impact energy, target thickness, density, yield strength and fracture toughness does not represent a unique solution.

According to the Buckingham Pi Theorem [41], two non-dimensional groups can be formed with five independent variables (impact energy, target thickness, density, yield strength and fracture toughness) and three units (length, mass, and time). Target thickness  $t$  is taken as the characteristic length ( $L^*$ ) term,  $\rho t^3$  is taken as the characteristic mass ( $M^*$ ) term and  $\rho^{1/2} t Y^{-1/2}$  is taken as the characteristic time ( $T^*$ ) term. The resulting non-dimensional groups are:

$$KE^* = \left( \frac{KE}{Y t^3} \right) \quad (1)$$

and

$$K_c^* = \left( \frac{K_c}{Y t^{1/2}} \right) \quad (2)$$

The resulting form of the non-dimensional fit is thus:

$$aKE^{*b}K_c^{*c} \quad (3)$$

where  $a$ ,  $b$ , and  $c$  are fitted coefficients obtained using a least-squares approach. The variation in target thickness (7 mm to 55 mm: 690 % difference) and kinetic energy (12 to 6,353 J: 52,800 % difference) will have a greater effect on  $a$ ,  $b$ , and  $c$  than density (23 % variation), yield strength (3 %) and fracture toughness (22 %). Material property selections, regardless of similarity, are considered justifiable and enable normalization of the experimental results.

### 3.1. % Ejected Mass, % Momentum and % Kinetic Energy

Shown in Figure 3a is the % excavated mass (defined as the ratio of ejecta mass to original target mass). Coefficient curve fits ( $a=4.50$ ,  $b=0.46$ ,  $c=-0.79$ ) are able to collapse the data well (coefficient of determination,  $R^2$ , of 0.88). Targets were weighed before and after each experiment and this determined the excavated mass. The dependence of % excavated mass on target and projectile size is not reflected in the current model. For example, values of % excavated mass would be much smaller if the target size was larger. Values range from 2% to 36% for the % excavated mass.

Shown in Figures 3b and c is the percentage of the change in projectile kinetic energy (or momentum) that is converted into the kinetic energy (or momentum) of ejected fragments tracked by algorithm. The ratio of tracked mass to excavated mass is used as scaling coefficient to estimate these values. Here, 85% to 95% of the total mass is captured by the algorithm. This is accomplished through with high resolution of fragment sizes via image enhancements (both of fine and larger fragments) and improved mass estimates. Coefficient fits of the non-dimensional groups ( $a=110.63$ ,  $b=0.47$ ,  $c=0.95$ ) for % momentum and ( $a=6.39$ ,  $b=0.54$ , and  $c=-0.21$ ) for % KE produce good fits of the data ( $R_{Momentum}^2=0.85$  and  $R_{KE}^2=0.80$ ). Values range from 2% to 25% for momentum conversion and 2% to 18 % for kinetic energy conversion.

Lastly, shown in Figure 3d is the ratio of summation of the kinetic energy in the y-direction to the summation of the kinetic energy in the x-direction. There is little correlation when coefficients are fitted, as evident by the lack of group overlapping. An average value of  $\sum KE_y / \sum KE_x = 0.037$  (highlighted with a line) reasonably describes all the experimental groups.

### 3.2. Length Scales: Distributions of Mass, Momentum and Kinetic Energy

Percentile values (i.e., 10<sup>th</sup>, 50<sup>th</sup> and 90<sup>th</sup>) of the distributions of mass, momentum and kinetic energy among length,  $L_i$ , are characterized in Figure 4. As an example,  $L_{50\% \text{ mass}}$  is the ejecta length at which 50% of the mass is contained above in a plot of cumulative distribution of mass plotted against length. Lengths for all sub-figures are normalized by target thickness,  $t$ , and are plotted for coefficient-fitted non-dimensional groups for the 50<sup>th</sup> percentile (Figure 4). The 10<sup>th</sup> and 90<sup>th</sup> percentile groups are fitted with an additional power-law function in the form of  $Kx^n$ , where  $x$  is the associated fitted non-dimensional groups on the x-axis. By definition, the fits for the 50<sup>th</sup> has the form  $1x^1$ . Fits of the non-dimensional groups are able to collapse the data well ( $R^2 > 0.77$  for all plots and all percentiles). For all cases, the 50<sup>th</sup> percentile values decrease at a faster rate than the other percentile values, indicating that the smaller and larger fragments are less sensitive to a change in input.

### 3.3. Cumulative Distributions of Mass, Momentum and Kinetic Energy among Ejecta Lengths

Cumulative distributions of mass, momentum and kinetic energy among length scales is examined in Figure 5. The cumulative distributions of mass among length, for example, is obtained by, first, computing the associated mass at each length value, and then integrating the probability distribution of mass among length. Lengths are normalized by their associated  $L_{50\%}$ . These are labelled as  $\% \text{Mass} > L/L_{50\% \text{ mass}}$ ,  $\% \text{Mom} > L/L_{50\% \text{ mom}}$ , and  $\% \text{KE} > L/L_{50\% \text{ KE}}$  in Figure 5. Distributions collapse well for the given normalizations. By definition, all data passes through the point (1, 50). Also shown in the figure are fitted functions in

the form of:

$$F\left(\frac{L}{L_i}\right) = C_1 e^{-\frac{L}{L_i}} \quad (4)$$

where  $C_1$  is a constant and  $L_i$  corresponding to either  $L_{50\% \text{ mass}}$ ,  $L_{50\% \text{ mom}}$ , or  $L_{50\% \text{ KE}}$ . Bounds for all  $L/L_i$  curve fits are taken as 0.3 to 4. Differentiating provides the functional form for the probability density distribution describing the mass, momentum and kinetic energy with respect to lengths:

$$p.d.f.\left(\frac{L}{L_i}\right) = -C_1 e^{-\frac{L}{L_i}} \quad (5)$$

Again, bounds for all  $L/L_i$  are 0.3 to 4.

#### 4. Discussion

The dynamic fragmentation of planetary materials during impact was examined for 76 data sets (four materials, target thicknesses: 7 mm to 55 mm, and impact energies of 10 J to 6,350 J.). A novel particle tracking algorithm was developed to measure ejecta size and velocity and the distribution of mass, momentum, and kinetic energy among ejecta lengths were characterized. These measurements represent the first of their kind in the literature. Two non-dimensional groups in the form:  $KE^* = (KE/Yt^3)$  and  $K_c^* = (K_c/Yt^{1/2})$  were developed and fitted with coefficients ( $a$ ,  $b$ , and  $c$ ) in the form:  $aKE^{*b}K_c^{*c}$  to develop semi-empirical models predicting % excavated mass, % ejecta momentum, and % ejecta kinetic energy. The models were able to collapse the data well (i.e., high value of  $R^2$ ). Values of  $b$  were 0.45 (mass), 0.47 (momentum) and 0.55 (kinetic energy). Holsapple [42] reports an exponent of 0.47 for cratering efficiency (i.e., amount of volume, or mass, that is ejected) for vertical impacts. The comparison for exca-

vated volume between experiments provides, perhaps, reason for expansion of the other semi-empirical models to vertical impacts.

The amount of ejecta kinetic energy/momentum to change in projectile kinetic energy/momentum was found to increase for increasing  $KE^*$ , ranging from 2% to 25% for momentum conversion and 2% to 18% for kinetic energy conversion. These represent a notable conversion of energy/momentum in the total energy partitioning and, based on work by Sanchidrian et al. [25] for blasting, seem reasonable. Momentum transfer is slightly greater due to relatively lower velocity ejection of the highly crushed materials for larger  $KE^*$ . Rotational energy has been shown to be two orders of magnitude smaller than translational kinetic energy [43] and is briefly considered. As an example from the current experiments, a 2 mm fragment rotating at 1 rad/s (estimated from video images) has a rotational kinetic energy of  $1.7E-10$  J. A similar fragment with a translational velocity of 0.5 m/s has a kinetic energy of  $1.3E-5$  J. This is five orders of magnitude in difference. An average value of  $\sum KE_y / \sum KE_x = 0.037$  (approximately 4%) was determined. This indicates that energy input into the lateral expansion of the debris field is minor in comparison to the energy dissipated in the streamwise expansion. The energy dissipated in the lateral direction is important in ejecta deposits formation on planetary surfaces during hypervelocity impacts, where the primary features of ejecta deposits are related to the material ejected at larger angles (vertical taken as  $0^\circ$ ).

Length scales during the dynamic fragmentation of geological materials were also examined. Fitting coefficients to non-dimensional terms provided reasonable collapse of the percentile data for the contribution of mass, momentum and kinetic energy among ejecta lengths. Length scales were found to decrease for increasing

$KE^*$  as a result of increased crushing (note the negative exponent for  $KE^*$ ). A functional form of the probability density distribution describing the distribution of mass, momentum and kinetic energy among the length scales was determined as:

$$p.d.f.\left(\frac{L}{L_i}\right) = -C_1 e^{-\frac{L}{L_i}} \quad (6)$$

The quantification of length scales containing mass, momentum, and kinetic energy contributions and the development of semi-empirical models should be helpful for the development of numerical models. In particular, prediction of important length scales to capture principal features of material ejection (e.g., 90 % of the fractured mass) is provided. This will enable better correlation between experiments and simulations to be realized [44]. With further development in, for example, fragment determining schemes and incorporating fragment interactions, numerical models can be used to extract energy dissipation (e.g., fracture, thermal, kinetic energy) among all length scales; like in turbulence [45].

#### *4.1. Comparison of the Distribution of Mass among Ejecta Lengths*

Median values of the distribution of mass among ejecta lengths are compared with prediction models by Grady [29], Glenn and Chudnovksy [30], Zhou et al. [34, 46] and Levy and Molinari [47] predicting average fragment size. In past experiments [2, 14, 32], number distributions of fragments are compared with theory. In experiments, it is not practical to measure all fragments, especially the sub  $\mu\text{m}$  fines. The consideration of distribution of mass among fragment size provides a reasonable approach for comparison among different experiments, or experimentation techniques (e.g., scratch testing [48], impact testing [14], expanding ring [47]). Grady's model to calculate average fragment size assumes that local

kinetic energy is converted to energy required to create new surfaces. The average fragment size,  $s_{Grady}$ , according to Grady [29] is calculated as:

$$s_{Grady} = \left( \frac{48G_c}{\rho\dot{\epsilon}^2} \right)^{1/3} \quad (7)$$

where  $\rho$  is the material density ( $\text{kg/m}^3$ ),  $\dot{\epsilon}$  is strain rate ( $\text{s}^{-1}$ ), and  $G_c$  is the fracture energy ( $\text{J/m}^2$ ).

Glenn and Chudnovsky [30] modified Grady's theory to account for strain energy at lower strain rates. They assumed that stored strain energy and local kinetic energy are converted to fracture energy. Their average fragment size be calculated from:

$$s_{GC} = 4\sqrt{\frac{3}{\alpha}} \sinh\left(\frac{\phi}{3}\right) \quad (8)$$

where

$$\phi = \sinh^{-1} \left[ \beta \left( \frac{3}{\alpha} \right)^{3/2} \right] \quad (9)$$

and

$$\alpha = \frac{3\sigma_c^2}{\rho E \dot{\epsilon}^2} \quad (10)$$

$$\beta = \frac{3G_c}{2\rho\dot{\epsilon}^2} \quad (11)$$

where  $E$  is Young's modulus (Pa) and  $\sigma_c$  is the strength of the material before failure (Pa).

Zhou et al. [34, 46] proposed the strain-rate dependent fragment size as:

$$s_{Zhou} = \frac{4.5EG_c}{\sigma_c^2} \left[ 1 + 0.77 \left( \frac{\dot{\epsilon}}{c\sigma_c^3/E^2G_c} \right)^{1/4} + 5.4 \left( \frac{\dot{\epsilon}}{c\sigma_c^3/E^2G_c} \right)^{3/4} \right]^{-1} \quad (12)$$

where  $c$  is the longitudinal speed of sound (m/s) in the material given by:

$$c = \sqrt{\frac{E}{\rho}} \quad (13)$$

Levy and Molinari [47] proposed the average fragment size be calculated as:

$$s_{LM} = t_0 C_{eff} \frac{3}{1 + 4.5 \left( E t_0 / \mu_{init} \right)^{2/3} \dot{\epsilon}^{2/3}} \quad (14)$$

where  $C_{eff}$  is effective longitudinal speed of sound and given as:

$$C_{eff} = c \left( \frac{2}{a + 1} \right)^{1/2} \left( \frac{\sigma_{c,min}}{\mu_{init}} \right)^{1/5} \quad (15)$$

where  $\sigma_{c,min}$  is the strength of the weakest link in a probability distribution of defects,  $\mu_{init}$  is the average strength,  $a$  is a scaling parameter depending on what type of distribution is chosen (e.g., Weibull, Gaussian), and  $t_0$  is a characteristic time (s) defined by Zhou et al. [46] as:

$$t_0 = \frac{EG_c}{c\sigma_c^2} \quad (16)$$

Shown in Figure 6 is the theoretical fragment size plotted against strain rate and the median values of experimental results. For comparison, a granitoid material is assumed. Values are taken as:  $\rho=2,700$  kg/m<sup>3</sup>,  $G_c= 70$  J/m<sup>2</sup> [49],  $E= 80$  GPa [49],  $\sigma_c=150$  MPa [50],  $\mu_{init}=\sigma_c/2$  (based on ratios used by Levy and Molinari [47]), and  $a=0.65$  [47]. Strain rate is estimated as the impact velocity over the target thickness and is varied. For comparison with experimental results,

this is assumed reasonable. Values are in range of those predicted by Grady [29] and decrease at rate similar (i.e., 1/3). Results from the particle tracking algorithm are consistent with those obtained using particle size analysis in Hogan et al. [14]. This provides support for estimating ejecta mass in a two-dimensional image of the debris cloud in this study.

## 5. Concluding Remarks

The dynamic fragmentation of planetary materials has been examined for various target materials, target thicknesses and impact velocities. Non-dimensional groups were formed and semi-empirical models developed to collapse data for % excavated mass, % ejecta momentum, and % ejecta kinetic energy. The amount of impact energy converted to kinetic energy of ejecta was found to increase from 2% to 18 % for increasing non-dimensional impact energy. This represents a notable conversion during total energy partitioning. Energy dissipated into expanding the field laterally was found to be small in comparison to the streamwise direction ( $\sum KE_y / \sum KE_x = 4\%$ ). Percentile length scales describing the contribution of mass, momentum and kinetic energy were also examined. Scales decrease for increasing impact energy. Fits of the non-dimensional groups provided reasonable collapse for the percentile values. Median values for the distribution of mass among ejecta lengths were found to agree reasonably with those predicted by Grady [29]. Lastly, the cumulative distributions of mass, momentum and kinetic energy among normalized lengths (i.e., normalized by 50 % length values) were quantified. Exponential function forms were found to fit all of the data over the range of  $L/L_i = 0.3$  to 4. These models provide predictive capabilities for the distribution of mass, momentum, and kinetic energy among ejecta lengths.

Substantial progress has been made in the theoretical and numerical treatment of the dynamic fragmentation of brittle materials. Future developments will require detailed experimental observations through quantification of important scales and energy partitioning. Improvements to experimental setups and methods will facilitate improvements in experimental analysis. Combined, functional forms, fitted non-dimensional groups and the extensive data set obtained in the current investigation provide a framework and predictive capabilities for future experimental studies. This will accommodate the next level of validation of numerical codes.

### **Acknowledgements**

This work was supported by a Natural Sciences and Engineering Research Council (NSERC) PGS-D scholarship to JDH and funding from NSERC, the Canada Research Chairs program and the Canada Foundation for Innovation to JGS. The authors would also like to thank the effort and contribution during the experimental phase of the study of Yannick Boehrer, David Bluntzer and Philippe Baumann at ISL. Planetary and Space Science Centre contribution 80.

### **References**

- [1] G. Hu, H. Otaki, M. Lin, An index of the tensile strength of brittle particles, *Minerals Engineering* 14 (10) (2001) 1199 – 1211.
- [2] J. D. Hogan, R. J. Rogers, J. G. Spray, S. Boonsue, Dynamic fragmentation of granite for impact energies of 6 to 28 J, *Engineering Fracture Mechanics* 79 (2012) 103 – 125.

- [3] J. S. Chester, F. M. Chester, A. K. Kronenberg, Fracture surface energy of the punchbowl fault, san andreas system, *Nature* 437 (2005) 133–136.
- [4] R. Buttner, P. Dellino, H. Raue, I. Sonder, B. Zimanowski, Stress-induced brittle fragmentation of magmatic melts: Theory and experiments, *Journal of Geophysical Research B: Solid Earth* 111 (8).
- [5] K. R. Housen, K. A. Holsapple, Ejecta from impact craters, *Icarus* 211 (1) (2011) 856 – 875.
- [6] B. Hermalyn, P. H. Schultz, M. Shirley, K. Ennico, A. Colaprete, Scouring the surface: Ejecta dynamics and the LCROSS impact event, *Icarus* 218 (1) (2012) 654 – 665.
- [7] P. Schultz, Shooting the moon: Constraints on lcross targeting, *LPI Contrib. 1327* (2006) 14–15.
- [8] V. Shuvalov, I. Trubetskaya, Numerical simulation of the LCROSS impact experiment, *Solar System Research* 42 (1) (2008) 1–7.
- [9] B. Paliwal, K. Ramesh, An interacting micro-crack damage model for failure of brittle materials under compression, *Journal of the Mechanics and Physics of Solids* 56 (3) (2008) 896 – 923.
- [10] F. Zhou, J.-F. Molinari, K. Ramesh, A cohesive model based fragmentation analysis: effects of strain rate and initial defects distribution, *International Journal of Solids and Structures* 42 (1819) (2005) 5181 – 5207.
- [11] F. Hild, C. Denoual, P. Forquin, X. Brajer, On the probabilistic to deter-

- ministic transition involved in a fragmentation process of brittle materials, *Computers and Structures* 81 (12) (2003) 1241 – 1253.
- [12] F. Zhou, J. Molinari, Dynamic crack propagation with cohesive elements. a methodology to address mesh dependency, *International Journal for Numerical Methods in Engineering* 59 (1) (2004) 1–24.
- [13] S. Maiti, K. Rangaswamy, P. H. Geubelle, Mesoscale analysis of dynamic fragmentation of ceramics under tension, *Acta Materialia* 53 (3) (2005) 823 – 834.
- [14] J. D. Hogan, J. A. Castillo, A. Rawle, J. G. Spray, R. J. Rogers, Automated microscopy and particle size analysis of dynamic fragmentation in natural ceramics, *Engineering Fracture Mechanics* 98 (0) (2013) 80 – 91.
- [15] D. W. Fuerstenau, A. Z. M. Abouzeid, The energy efficiency of ball milling in comminution, *International Journal of Mineral Processing* 67 (1-4) (2002) 161 – 185.
- [16] D. Tromans, Mineral comminution: Energy efficiency considerations, *Minerals Engineering* 21 (8) (2008) 613 – 620.
- [17] D. Tromans, J. Meech, Fracture toughness and surface energies of minerals: Theoretical estimates for oxides, sulphides, silicates and halides, *Minerals Engineering* 15 (12) (2002) 1027–1041.
- [18] D. Tromans, J. Meech, Fracture toughness and surface energies of covalent minerals: Theoretical estimates, *Minerals Engineering* 17 (1) (2004) 1–15.

- [19] R. Woodward, W. Gooch, Jr, R. O'Donnell, W. Perciballi, B. Baxter, S. Pat-  
tie, A study of fragmentation in the ballistic impact of ceramics, *International  
Journal of Impact Engineering* 15 (5) (1994) 605 – 618.
- [20] J. D. Hogan, J. G. Spray, R. J. Rogers, S. Boonsue, G. Vincent, M. Schneider,  
Micro-scale energy dissipation mechanisms during dynamic fracture in nat-  
ural polyphase ceramic blocks, *International Journal of Impact Engineering*  
38 (12) (2011) 931 – 939.
- [21] S. P. Gross, J. Fineberg, M. Marder, W. D. McCormick, H. L. Swinney,  
Acoustic emissions from rapidly moving cracks, *Phys. Rev. Lett.* 71 (19)  
(1993) 3162–3165.
- [22] D. Braslau, Partitioning of energy in hypervelocity impact against loose sand  
targets, *Journal Of Geophysical Research* 75 (1970) 3987.
- [23] F. C. Bond, The third theory of comminution, *Transactions  
SME/AIME* (193) (1952) 484 – 494.
- [24] E. Sharon, S. P. Gross, J. Fineberg, Energy dissipation in dynamic fracture,  
*Phys. Rev. Lett.* 76 (12) (1996) 2117–2120.
- [25] J. A. Sanchidrin, P. Segarra, L. M. Lopez, Energy components in rock blast-  
ing, *International Journal of Rock Mechanics and Mining Sciences* 44 (1)  
(2007) 130 – 147.
- [26] D. Gault, E. Heitowit, The partition of energy for hypervelocity impact  
craters formed in rock, *Proc. 6th Hypervelocity Impact Symp* (1963) 419–  
456.

- [27] N. Mott, Fragmentation of shell cases, Technical Report A189: 300308, Proceedings of the Royal Society (1947).
- [28] D. Grady, M. Kipp, Geometric statistics and dynamic fragmentation, *Journal of Applied Physics* 58 (3) (1985) 1210–1222.
- [29] D. E. Grady, Length scales and size distributions in dynamic fragmentation, *International Journal of Fracture* 163 (1–2) (2009) 85–99.
- [30] L. A. Glenn, A. Chudnovsky, Strain and energy effects on dynamic fragmentation, *Journal of Applied Physics* 59 (4) (1986) 1379 –1380.
- [31] W. Drugan, Dynamic fragmentation of brittle materials: analytical mechanics-based models, *Journal of the Mechanics and Physics of Solids* 49 (6) (2001) 1181 – 1208.
- [32] O. Miller, L. Freund, A. Needleman, Modeling and simulation of dynamic fragmentation in brittle materials, *International Journal of Fracture* 96 (2) (1999) 101–125.
- [33] V. Shenoy, K.-S. Kim, Disorder effects in dynamic fragmentation of brittle materials, *Journal of the Mechanics and Physics of Solids* 51 (1112) (2003) 2023 – 2035.
- [34] F. Zhou, J. F. Molinari, K. Ramesh, Analysis of the brittle fragmentation of an expanding ring, *Computational Materials Science* 37 (1-2) (2006) 74 – 85.
- [35] J. Hogan, J. Spray, R. Rogers, G. Vincent, M. Schneider, Dynamic fragmentation of natural ceramic tiles: Ejecta measurements and kinetic conse-

quences, *International Journal of Impact Engineering* (2013) Accepted Feb 2013.

- [36] Mathworks, 2013 Matlab User Manual.
- [37] A. Piekutowski, R. Andrews, H. Swift, Studying small-scale explosive cratering phenomena photographically, *Int Congr on High Speed Photogr (Photonics)*, 12th 97 (1977) 177–183.
- [38] M. J. Cintala, L. Berthoud, F. Horz, Ejection-velocity distributions from impacts into coarse-grained sand, *Meteoritics and Planetary Science* 34 (4) (1999) 605–623.
- [39] S. Yamamoto, T. Kadono, S. Sugita, T. Matsui, Velocity distributions of high-velocity ejecta from regolith targets, *Icarus* 178 (1) (2005) 264 – 273.
- [40] T. Michikami, K. Moriguchi, S. Hasegawa, A. Fujiwara, Ejecta velocity distribution for impact cratering experiments on porous and low strength targets, *Planetary and Space Science* 55 (12) (2007) 70 – 88.
- [41] B. R. Munson, D. F. Young, T. H. Okiishi, *Fundamentals of fluid mechanics*, Wiley, 1990 - 843 pages.
- [42] K. A. Holsapple, The scaling of impact processes in planetary sciences, *Annual Review of Earth and Planetary Sciences* 21 (1993) 33–37.
- [43] A. Fujiwara, Energy partition into translational and rotational motion of fragments in catastrophic disruption by impact: An experiment and asteroid cases, *Icarus* 70 (3) (1987) 536 – 545.

- [44] M. Jutzi, P. Michel, W. Benz, D. C. Richardson, Fragment properties at the catastrophic disruption threshold: The effect of the parent body's internal structure, *Icarus* 207 (1) (2010) 54 – 65.
- [45] J.-D. Fournier, U. Frisch,  $d$ -dimensional turbulence, *Phys. Rev. A* 17 (1978) 747–762.
- [46] F. Zhou, J. F. Molinari, K. T. Ramesh, Effects of material properties on the fragmentation of brittle materials, *International Journal of Fracture* 139 (2006) 169–196.
- [47] S. Levy, J. Molinari, Dynamic fragmentation of ceramics, signature of defects and scaling of fragment sizes, *Journal of the Mechanics and Physics of Solids* 58 (1) (2010) 12 – 26.
- [48] J. D. Hogan, R. J. Rogers, J. G. Spray, S. Boonsue, Fracture and fragmentation of quartz and albite during single-diamond sliding-point contact, *Engineering Fracture Mechanics* 96 (0) (2012) 165 – 178.
- [49] H. Ai, T. Ahrens, Simulation of dynamic response of granite: A numerical approach of shock-induced damage beneath impact craters, *International Journal of Impact Engineering* 33 (1-12) (2006) 1 – 10.
- [50] J. G. Spray, Frictional melting processes in planetary materials: From hypervelocity impact to earthquakes, *Annual Review of Earth and Planetary Sciences* 38 (1) (2010) 221–254.
- [51] M. A. Lange, T. J. Ahrens, M. B. Boslough, Impact cratering and spall failure of gabbro, *Icarus* 58 (3) (1984) 383 – 395.

**List of Tables**

1	Material type, number of experiments, and impact velocity and kinetic energy. . . . .	29
2	Density, yield strength and fracture toughness for the materials. Values taken from [49–51]. . . . .	29

## List of Figures

1	(a) Tonalitic granitoid (7 mm to 40 mm), (b) syenitic granitoid, (c) coarser grained monzonitic granitoid (55 mm), and (d) gabbro material (10 mm). Projectile types are shown in (e). . . . .	30
2	(a) High-speed video images with (b) enhancements to render the fragments more distinguishable. Examples of velocity vectors and the co-ordinate system in shown in (c). . . . .	31
3	Plots of fitted non-dimensional groupings versus: (a) % excavated mass, (b) % ejecta momentum, (c) % ejecta kinetic energy, and (d) $\sum KE_y / \sum KE_x$ . KE: Kinetic energy. . . . .	32
4	$10^{th}$ , $50^{th}$ and $90^{th}$ percentile values of normalized length scales plotted against coefficient fitted non-dimensional groups: (a) $L_{mass}/L^*$ , (b) $L_{mom}/L^*$ , and (c) $L_{KE}/L^*$ . . . . .	33
5	Cumulative distribution plots of: (a) $\%Mass > L/L_{50\% mass}$ , (b) $\%Mom > L/L_{50\% mom}$ , and (c) $\%KE > L/L_{50\% KE}$ . . . . .	34
6	Comparison of $L_{50\% mass}$ with theories by Glenn and Chudnovsky [30], Grady [29], Levy and Molinary [47], and Zhou et al.[34]. . . . .	35

Table 1: Material type, number of experiments, and impact velocity and kinetic energy.

Material Type	Number of Experiments	Target Thickness (mm)	Impact Velocities (m/s)	Impact Energies (J)
Tonalitic granitoid	6	7	46 to 92	66 to 262
Tonalitic granitoid	11	10 (series 1)	20 to 95	12 to 280
Tonalitic granitoid	7	10 (series 2)	152 to 240	716 to 1,786
Tonalitic granitoid	11	20	35 to 202	38 to 1,265
Tonalitic granitoid	7	30	96 to 284	286 to 2,500
Tonalitic granitoid	6	40	171 to 269	906 to 2,243
Gabbro	19	10	26 to 100	21 to 305
Syenitic granitoid	5	55	347 to 550	2,529 to 6,353
Coarse monzonitic granitoid	4	55	250 to 313	1,938 to 3,037

Table 2: Density, yield strength and fracture toughness for the materials. Values taken from [49–51].

Material Type	density ( $\rho$ : kg/m <sup>3</sup> )	Yield Strength ( $Y$ : MPa)	Fracture Toughness ( $K_c$ : MPa $\sqrt{m}$ )
Gabbro	3200	150	2.2
Tonalitic granitoid	2800	148	1.8
Syenitic granitoid	2700	148	1.8
Monzonitic granitoid	2600	145	1.8

Fig 1. Target and Projectiles

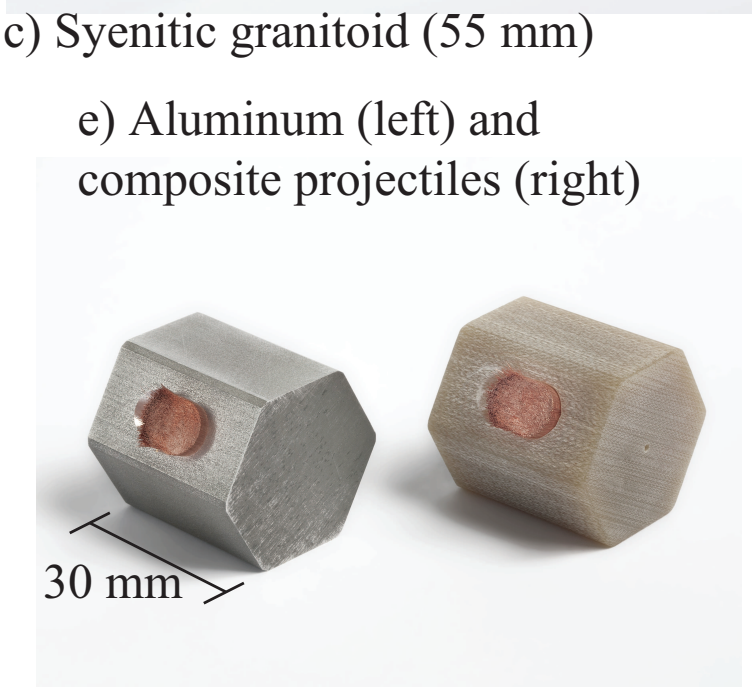


Fig 2. Particle tracking methods

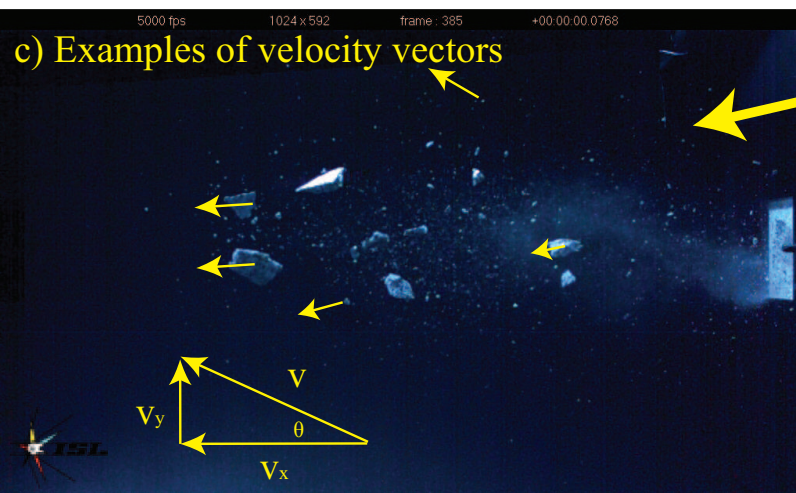
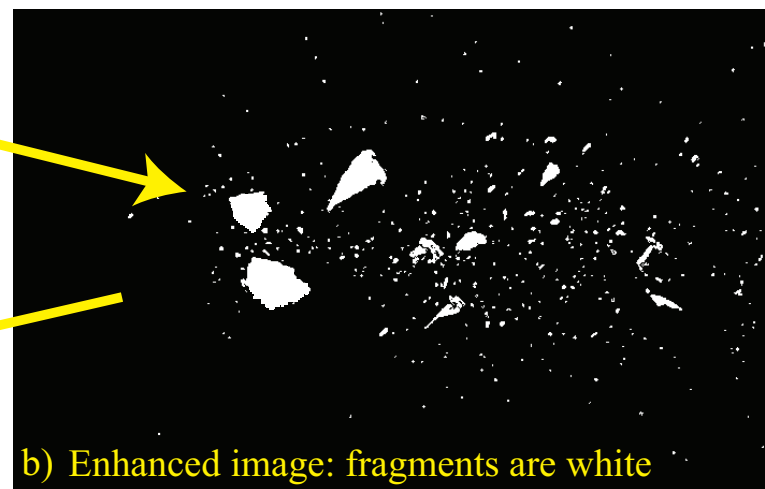
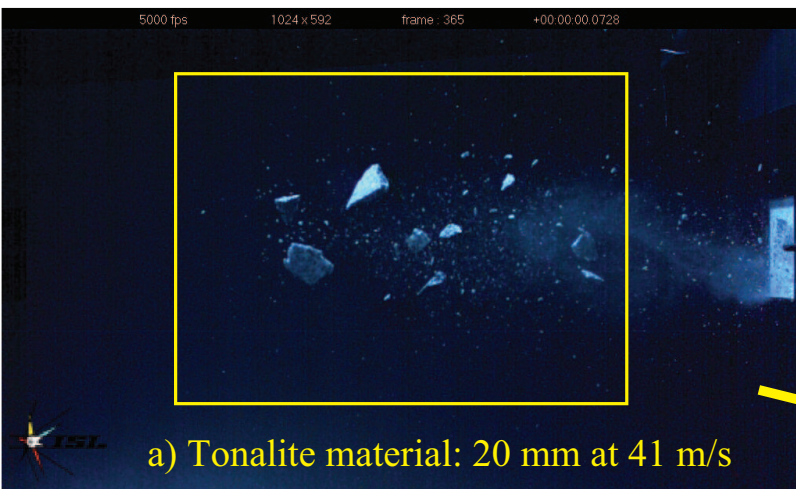


Fig 3. Non-dimensional group fits of data

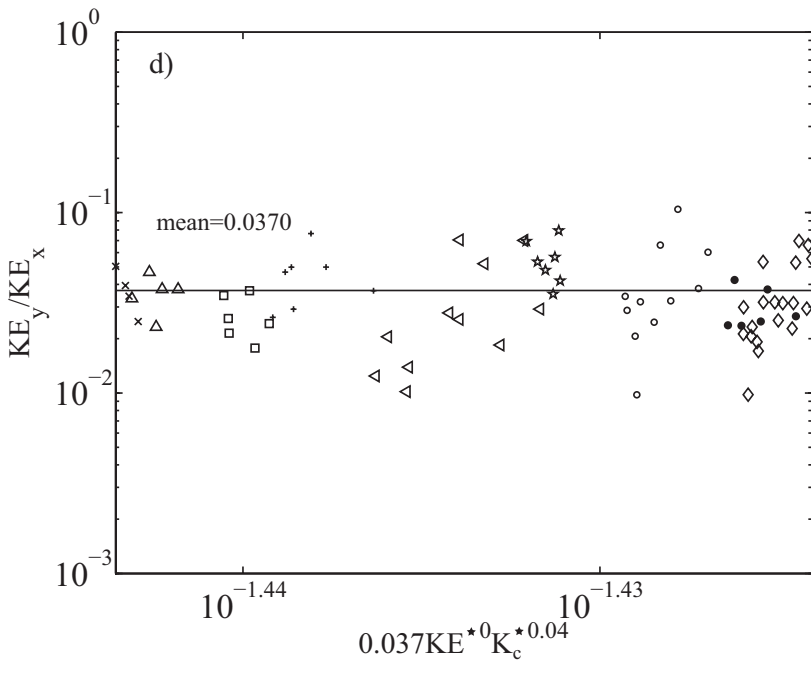
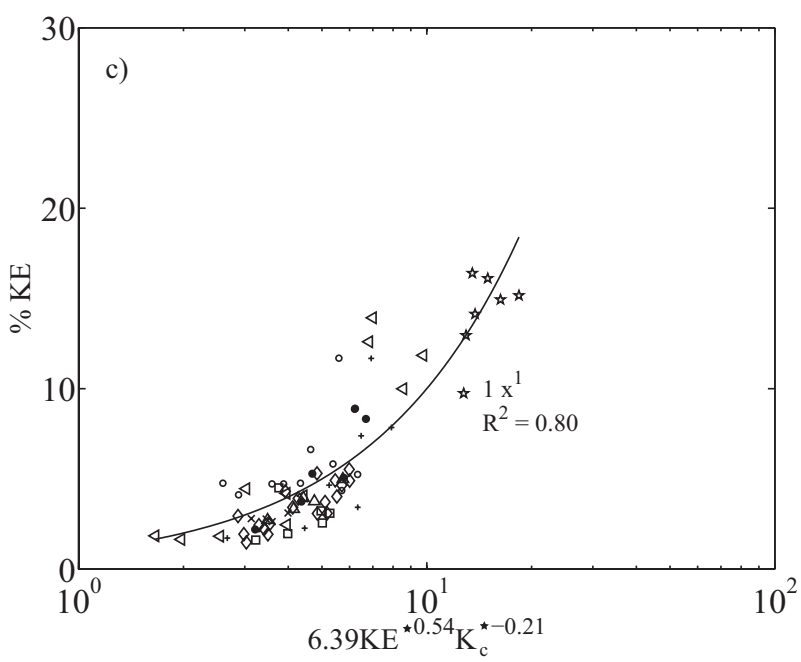
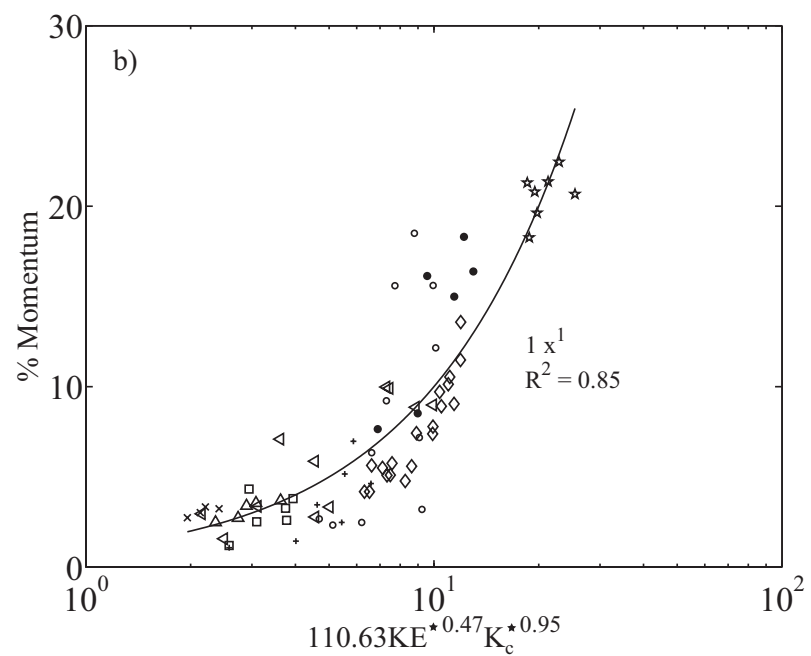
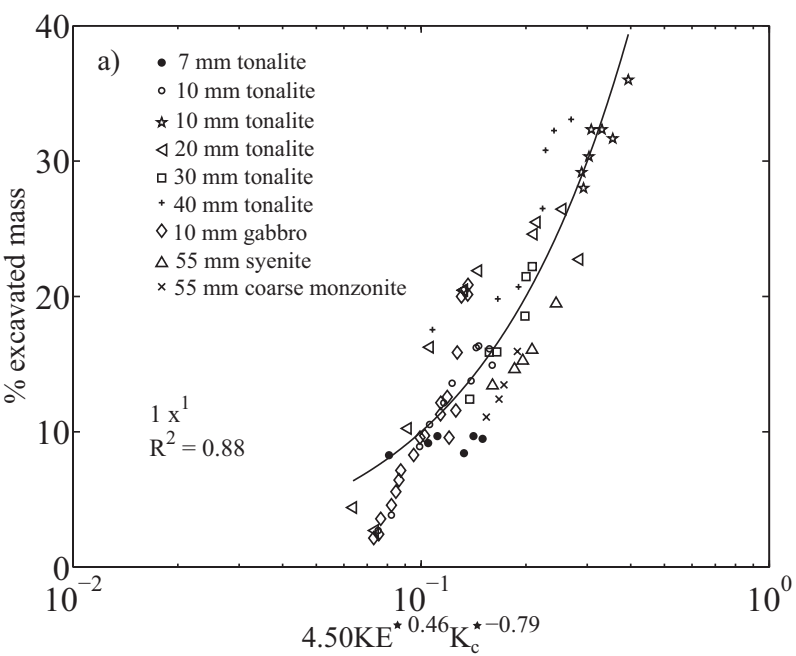
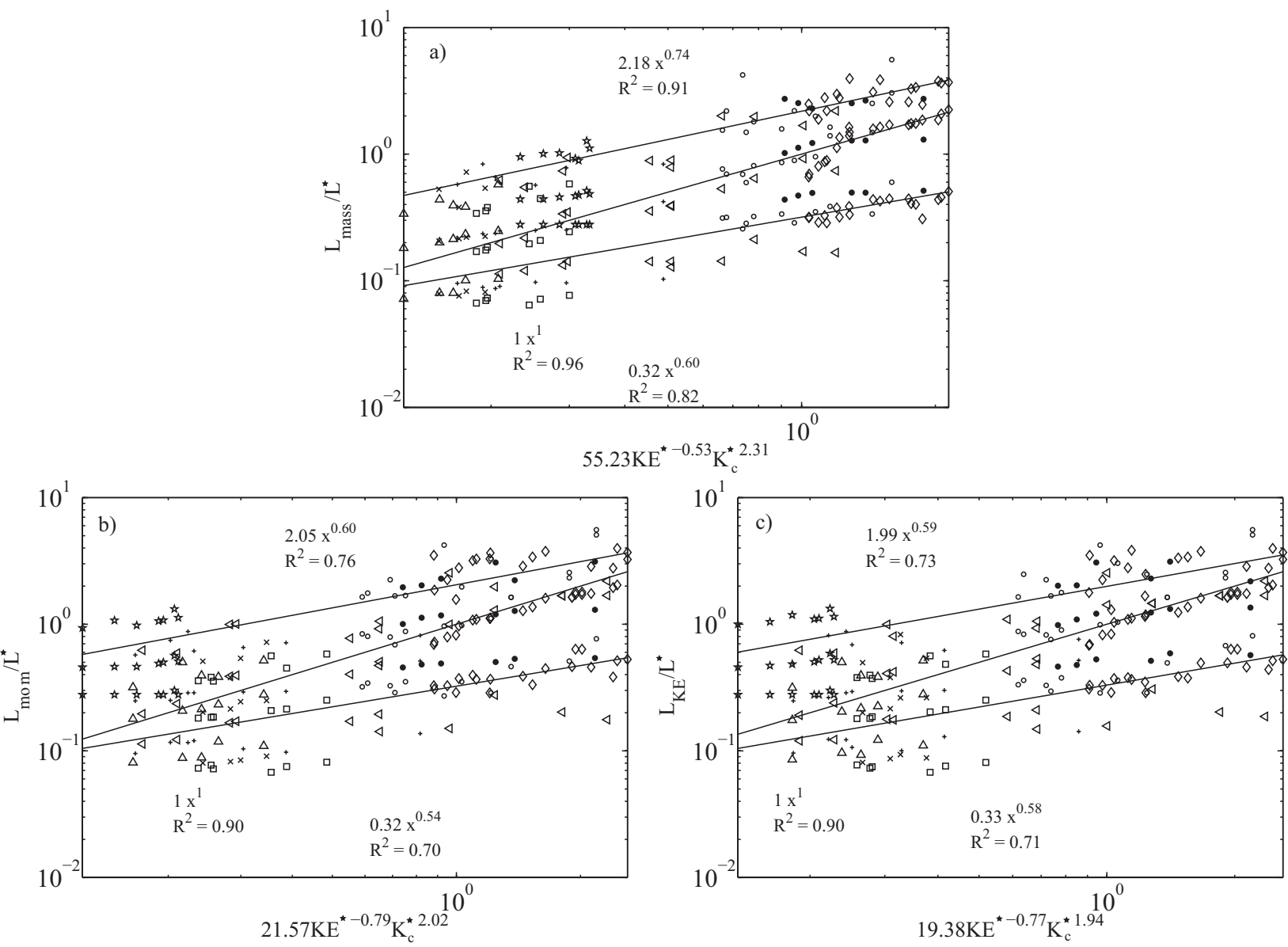


Fig 4. Percentiles of mass, momentum and KE among length



**Fig 5. Distribution of mass, momentum and KE among length**

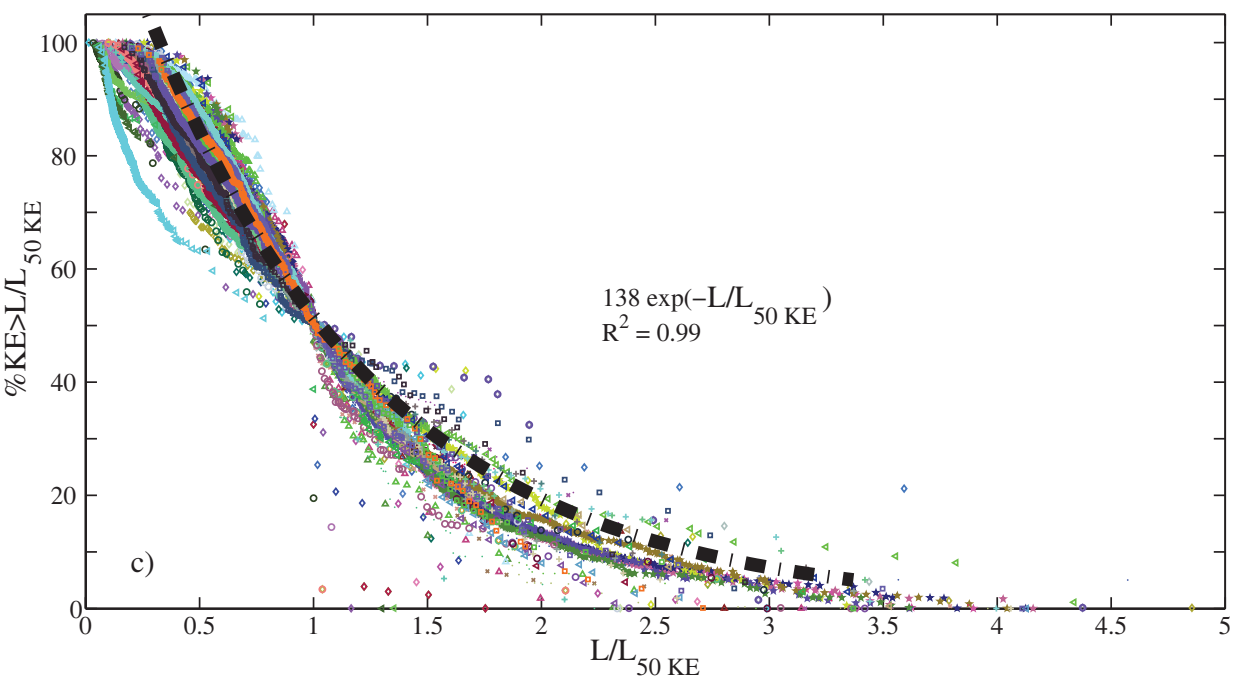
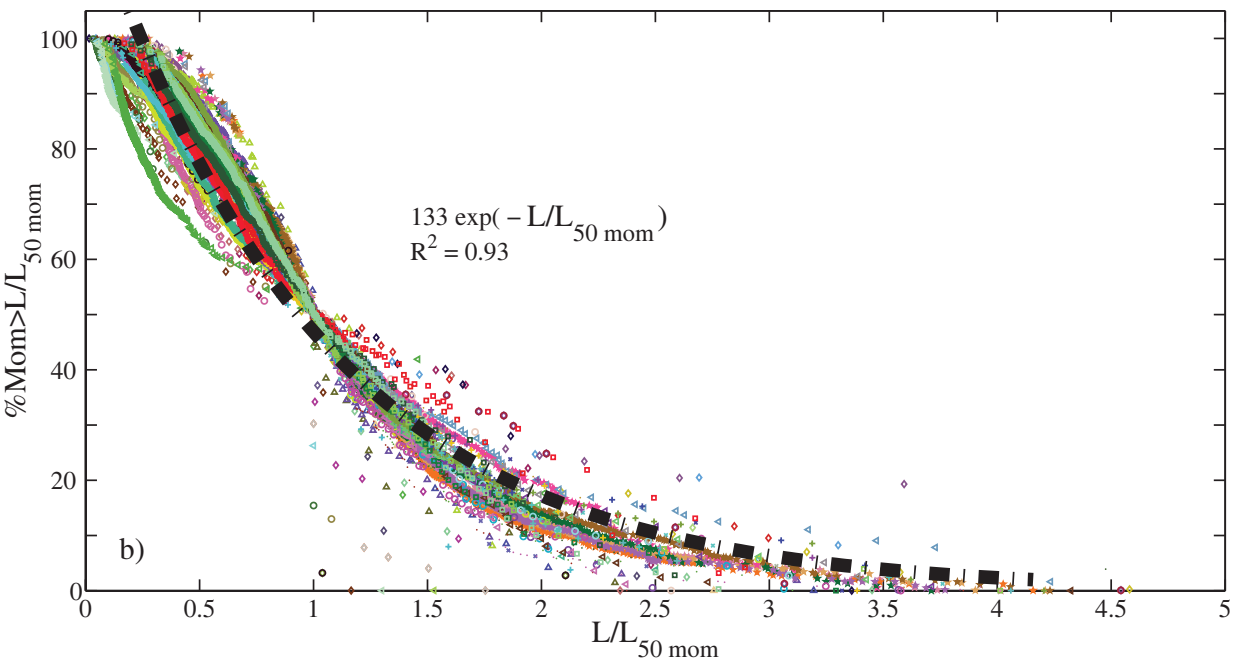
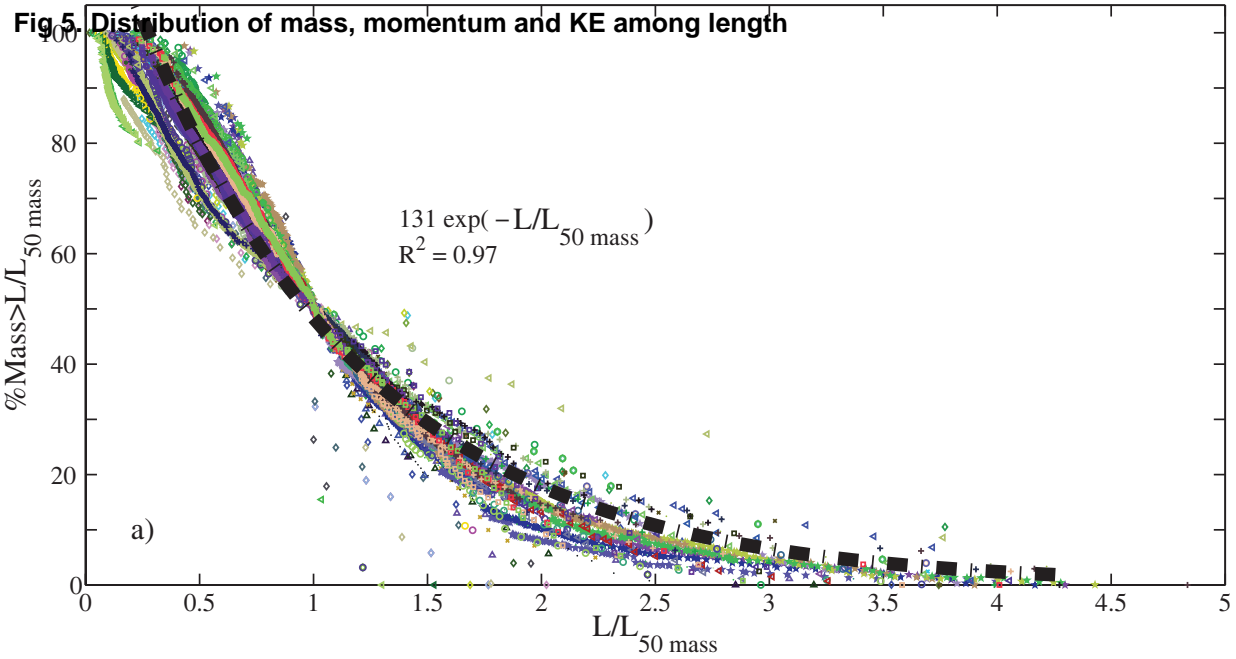


Fig 6. Comparison of experimental results with theory

